J. Fluid Mech. (1998), *vol.* 375, *pp.* 85–111 Printed in the United Kingdom

Flow behind castellated blunt-trailing-edge aerofoils at supersonic speeds

By E. C. MAGI[1] AND S. L. GAI[2]

[1] The Defence Science and Technology Organisation, Salisbury, South Australia

[2] University College, UNSW, Australian Defence Force Academy, Canberra, ACT 2600, Australia

(Received 10 January 1996 and in revised form 24 June 1998)

A study of the near-wake flow of castellated blunt-trailing-edge aerofoils at a Mach number of 2 was conducted to understand the nature of the flow and the mechanisms of base pressure recovery. The investigation has shown that strong gradients exist in the spanwise direction and that the formation of the wake recompression shock occurs further away from the wake axis. Also, the wake neck is broader and diffused. Detailed quantitative data involving pressure measurements, schlieren and holographic interferometry, and laser transit velocimetry, are presented. A theoretical model to predict the mean base pressure on a castellated base is also proposed. Comparison with experimental data shows that the model provides a qualitative description of the flow behind a castellated base at supersonic speeds.

1. Introduction

Although a blunt-trailing-edge aerofoil has advantages at transonic and supersonic speeds (Holder 1964), it creates high base drag at subsonic speeds due to periodic vortex shedding (Roshko 1993). Techniques such as splitter plates and base bleed have been used in the past to control or eliminate this problem (Bearman 1965, 1967). A passive technique, that of castellating a blunt trailing edge, thus providing a discontinuous separation line, has been shown to be quite effective in recent years (Tanner 1972; Pollock 1972; Gai & Sharma 1981).

However, very little is known about the behaviour of a castellated blunt-trailing-edge aerofoil at supersonic speeds although some preliminary (unpublished) work in the mid seventies (Hosking & Self 1974; Steen 1975) suggested that some base drag reductions are achievable. However, the mechanism of the base pressure recovery and the physics of the wake flow of such configurations is not yet fully understood. The subject has particular relevance to the design of supersonic/hypersonic aircraft and missiles and wake flows in turbo-machinery.

A study of the near-wake flow of castellated blunt-trailing-edge aerofoils at a supersonic free-stream Mach number of 2 was therefore undertaken to understand the mechanism of base pressure recovery. This paper presents some of the results obtained during the course of this study.

2. Experimental arrangement, models, and techniques

The experiments were conducted in a blow-down supersonic wind tunnel of cross-section 155 mm (height) $\times$ 90 mm (width) at a Mach number of 2 and Reynolds number based on free-stream conditions and chord length L in the range $2 \times 10^6 < Re_L < 9 \times 10^6$. The models had a wedge-shaped leading edge followed by a flat plate with

a blunt trailing edge. The base height h for all the models was 6 mm. The availability of only side test section windows meant that two sets of models had to be made – one to study the streamwise development of the flow and the other to examine the spanwise flow behind the base. Those constructed to look at the streamwise flow were horizontally mounted and had a chord length of 130 mm. Those constructed to study spanwise features of the flow were vertically mounted and had a chord of 75 mm.

Before describing the castellated blunt-trailing-edge aerofoils used in this investigation, an explanation of the terminology used is in order. Figure 1(a, b) shows the geometry of a rectangular castellated trailing edge. The term *trailing edge* here refers to the rear end of the aerofoil containing the base geometry. Referring to figure 1(a), a denotes the depth of the recess, b_1 is the width of the recess, b_2 is the width of the projection, and h is the base height at the trailing edge. When $b_1 = b_2$ (as is the case in the present investigation), the subscript may be dropped and we can define the aspect ratio A of the castellation element as the width b divided by the depth a.

The coordinate system for the castellated trailing-edge geometry (figure 1b) is defined such that in the streamwise direction $x = 0$ denotes the base of the projection; in the transverse direction $y = 0$ denotes the centreline of the base/wake; and along the spanwise direction $z = 0$ is the centreline of the recess (see also figure 17).

It is known that the width-to-depth ratio of rectangular castellations strongly influences the base pressure recovery in subsonic flows. The investigations of Tanner (1972) and Pollock (1972) found that maximum base pressure recovery was achieved with $b/h = 3.9$ and $a/h = 1.9$, and $b/h = 3.3$ and $a/h = 2$, respectively. Subsequent investigations by Petrusma & Gai (1994) showed that for maximum base pressure recovery, $b/h = 4$ and $a/h = 2$.

Also, the theoretical calculations of Pierrehumbert & Widnall (1982) have shown that the spanwise wavelength of a naturally occurring streamwise 'wiggle' in a free shear layer is 2/3 of the spacing of the undisturbed vortices which, with a wave height of the order of the base height, suggests an aspect ratio around unity. Experiments by Briedenthal (1980) to study the effects of strong three-dimensional perturbations to a planar wake from a blunt base were also conducted with rectangular segments whose aspect ratio was unity.

It was therefore of interest to see how the aspect ratio of castellations affected the base pressure recovery at supersonic speeds. Castellations of aspect ratio varying form 2/3 to 3 were therefore examined, and, various combinations of width (b) and depth (a) were tested to yield different aspect ratios as follows: (a) horizontally mounted models with spacing ratios $b/h \times a/h = 3 \times 1; 3 \times 2; 3 \times 3; 2 \times 1$; and 1×1; (b) vertically mounted models with spacing ratios $b/h \times a/h = 3 \times 1;\ 3 \times 2;\ 3 \times 3;\ 2 \times 1;\ 2 \times 2;\ 2 \times 3$. Figure 1($c$) shows a photograph of one of the models.

To measure base pressures on projections and recesses, pressure tappings were provided along the spanwise (z) axis of the base which were connected to a pressure transducer via a scanivalve and were then logged into a computer for data processing. Most models had three pressure tappings on each of the recess and projection. On some models, however, the recess and projection were equipped with up to seven pressure tappings each to examine the detailed pressure variations. Sufficient pressure tappings were also located on the base in the transverse direction to examine the variation of the base pressure across the thickness of the base. As explained later in the discussion of results, entrainment of the fluid from the top of the projection and into the recess is an important feature of the flow. To examine this, therefore, pressure tappings were also provided on the top surface of the projection elements on some models.

To compare with the results of a castellated trailing edge, experiments were also

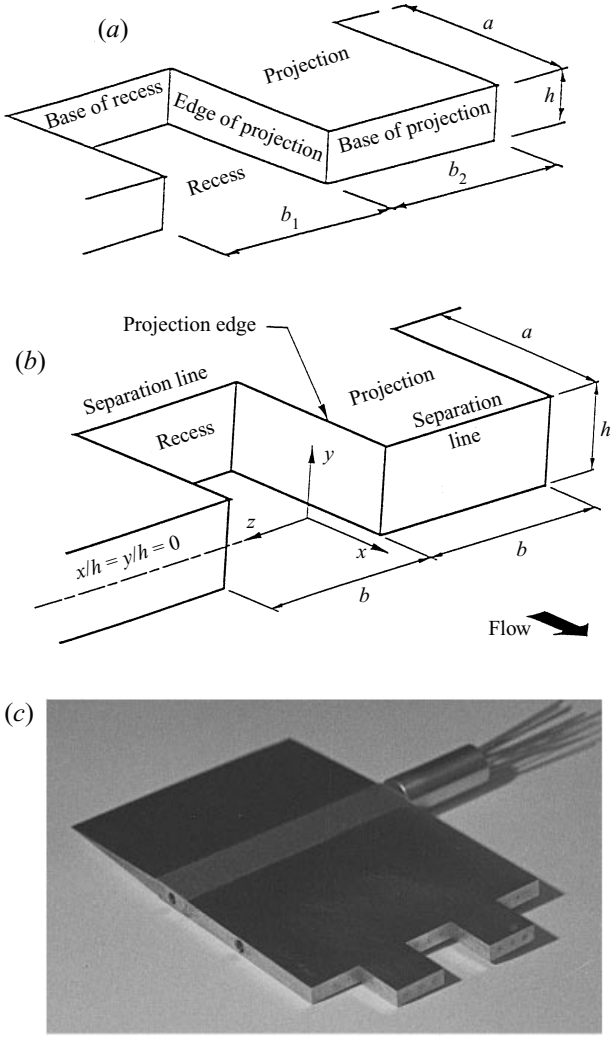

FIGURE 1. (*a*) Nomenclature and geometry of castellations. (*b*) Coordinate system. (*c*) A typical castellated blunt-trailing-edge model.

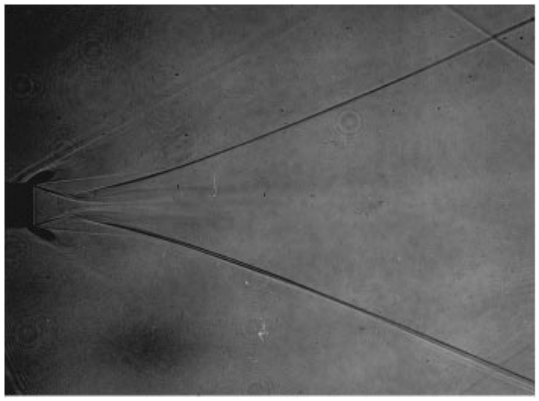

FIGURE 2. Shadowgraph showing flow behind a plain blunt-trailing-edge model.

conducted with a plain blunt trailing edge. This had a base height of 6 mm, a chord of 130 mm, and was equipped with pressure tappings on the base.

The techniques employed for acquisition of data consisted of base pressure measurements, pitot traverses in the near wake, schlieren and shadow photography, holographic interferometry, and laser transit velocimetry (LTV). Taken together, they have provided an extensive and detailed picture of the complicated flow behind castellated blunt-trailing-edge aerofoils at supersonic speeds.

3. Results and discussion

3.1 *The plain blunt trailing edge*

The supersonic flow behind a two-dimensional plain base is now fairly well understood (Chapman 1951; Korst 1956; Tanner 1984). It can be conveniently divided into various flow regimes. Briefly, the separating flow undergoes an expansion around the corner, forming a re-circulation region behind the base. A free shear layer separates the re-circulation region from the expansion fan. The flow re-compresses approximately one to two base heights downstream of the base forming a wake neck and a wake shock which then turns the flow back to the free-stream direction. The expansion fan is sometimes terminated by a lip shock as seen in figure 2. The lip shock re-compresses the over-expanded flow to the base pressure. Hama (1968) has shown that the location and strength of the lip shock depend on the Reynolds number, the Mach number and the base geometry.

It is known that for a given Mach number and geometry, the base pressure is a function of the Reynolds number Re_L. Figure 3 shows the base pressure variation with Reynolds number obtained in this investigation. The variation in Reynolds number was achieved by varying the stagnation pressure. These results suggest that transition region lies in the range $3\times10^6 < Re_L < 7\times10^6$. Hama (1968) has suggested that the transition from laminar to turbulent flow in the near wake moves upstream from the reattachment region towards the separation corner as the Reynolds number of the flow increases. This also results in a decrease in the base pressure. For Reynolds numbers below 3×10^6 and above 7×10^6 the base pressure was seen to correlate well with Chapman's correlating parameters for laminar and turbulent flows respectively. For most experimental conditions, however, both for the plain and the castellated base, the chord Reynolds number was around 9×10^6 so that the separating boundary layer was turbulent. A boundary layer traverse 2 mm upstream of the trailing edge showed that this was indeed the case. The boundary layer was 2.45 mm thick and approximately followed the 1/7th power law profile.

The mean base pressure coefficient obtained from the measurements was -0.227 and it agrees very well with the theoretical prediction of -0.23 based on the Chapman–Korst theory as well as the theory of Tanner (1984). The base pressure coefficient is defined as $C_{p_b} = (p_b - p_\infty)/q_\infty$, where p_b is the base pressure, p_∞ is the free-stream static pressure, and q_∞ is the free-stream dynamic pressure. The base pressure varied slightly with the stagnation pressure (P_0) of the wind tunnel. During the tunnel run, the stagnation pressure variation $\mathrm{d}P_0/\mathrm{d}t$ was typically of the order of 20 kPa s^{-1}. This gave an accuracy in the measurement of the base pressure coefficient of $C_{p_b} \pm 0.005$.

3.2. *The castellated trailing edge*

The study of the flow behind a castellated trailing edge was done in four parts: first, the base pressure measurements; second, schlieren and shadow photography, and holographic interferometry viewing streamwise and spanwise; third, Pitot traverses in

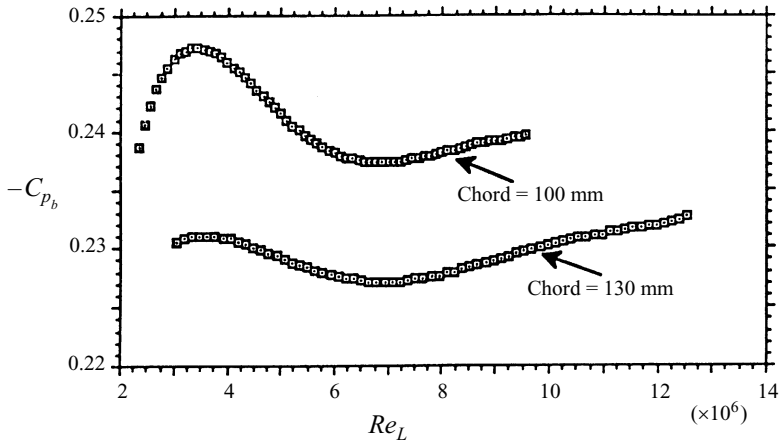

FIGURE 3. Base pressure variation with Reynolds number.

the wake; and finally, laser two-focus velocimetry. In addition, oil flow studies were also conducted, especially to investigate the finer details of the flow on the projection elements and in the recesses.

3.2.1. *Base pressure measurements*

Figure 4 shows some examples of pressure distributions obtained with castellated blunt trailing edges. They are seen to be quite different from that of the plain blunt base (also shown). We note strong spanwise gradients caused by the segments and that pressures within the recess and on the projection are independent of each other. The pressures on the two end recesses are seen to be influenced by the tunnel sidewalls. We also note that the pressures within the recess are generally higher than those on the projections. This feature is unlike that observed in subsonic flow (Tanner 1972; Petrusma & Gai 1994). The mean base pressure coefficient for the whole span, obtained by graphical integration, is also indicated on the figure.

Overall, the mean base pressure coefficient of the castellated blunt trailing edge is higher than that of the plain blunt trailing edge, resulting in some pressure recovery. For the examples shown in figure 4, it is between 3 % and 15 % depending on the aspect ratio of the castellations.

While the results shown in figure 4 indicate the general trend of pressure variation across the span of a castellated blunt trailing edge, it is important to ascertain the detailed flow behaviour across individual elements. Figure 5 shows such details on a projection element of castellations of different aspect ratio. We note that large spanwise gradients exist with high pressures at the centre and low pressures at the recess/projection boundary. These gradients are quite strong for $A > 1$. We also note that with decrease in aspect ratio, the gradients are significantly reduced and at the same time the mean base pressure is increased. When $A < 1$, the pressure distribution is almost flat and the base pressure is maximum. Another feature of these pressure distributions is that they are remarkably symmetrical.

The recess pressure distributions behaved in a similar manner in that the mean base pressure of the recess also increased with decrease in aspect ratio. However, there seemed to be some dependence on the segment width in that the gradients across the span of the recess were somewhat larger for the smaller width ($b/h = 2$) than for the larger one ($b/h = 3$).

Figure 6 shows the pressure distribution on the top surface of a projection element

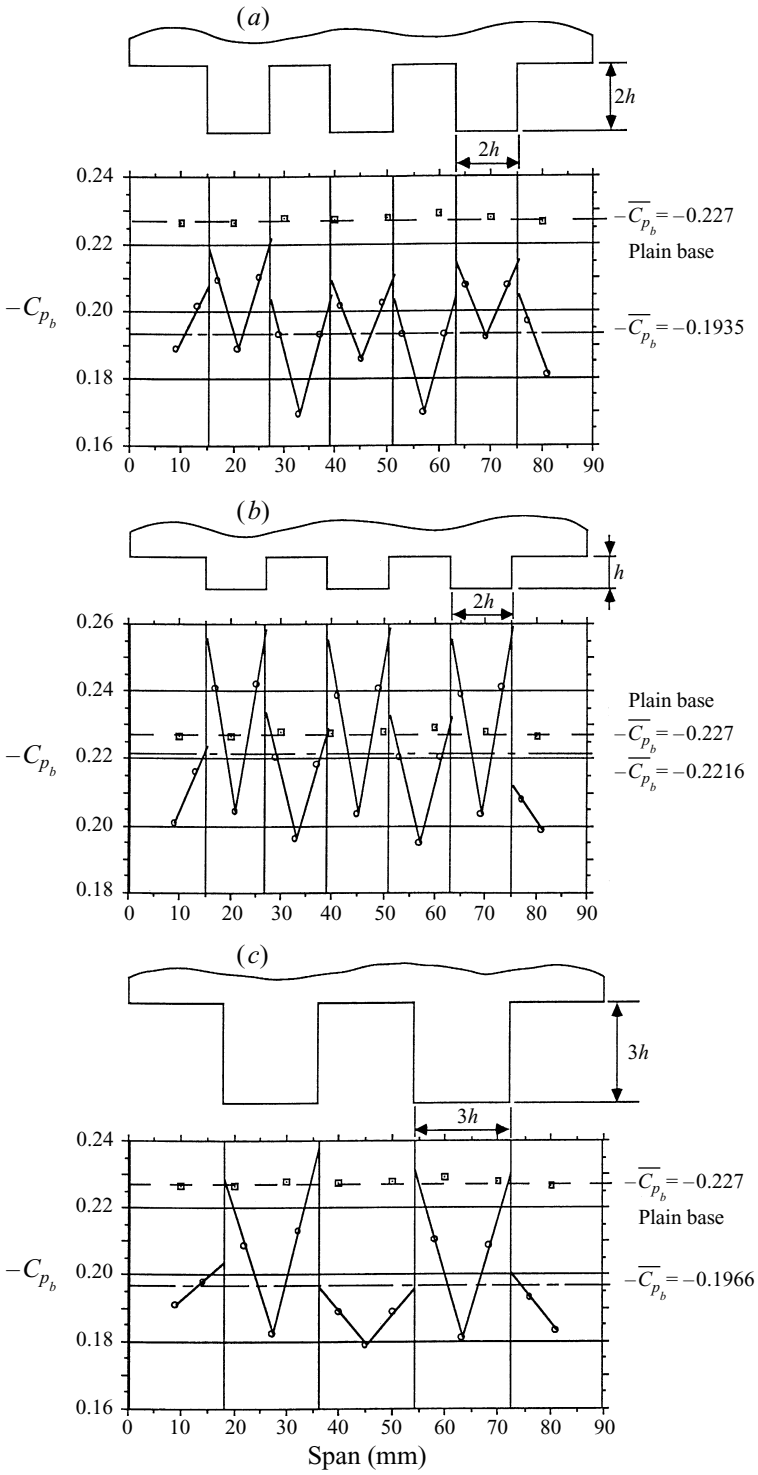

FIGURE 4. Spanwise variation of base pressure with a castellated trailing edge: (*a*) $A = 1$, $a/h = 2$; (*b*) $A = 2$, $a/h = 1$; (*c*) $A = 1$, $a/h = 3$.

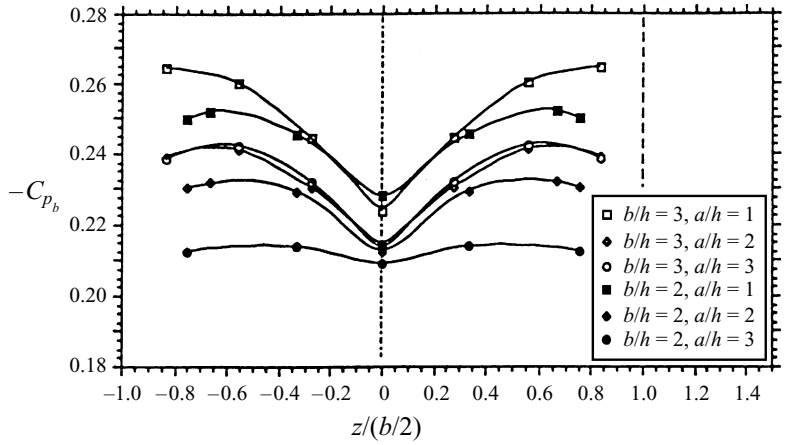

FIGURE 5. Pressure distribution across a projection element.

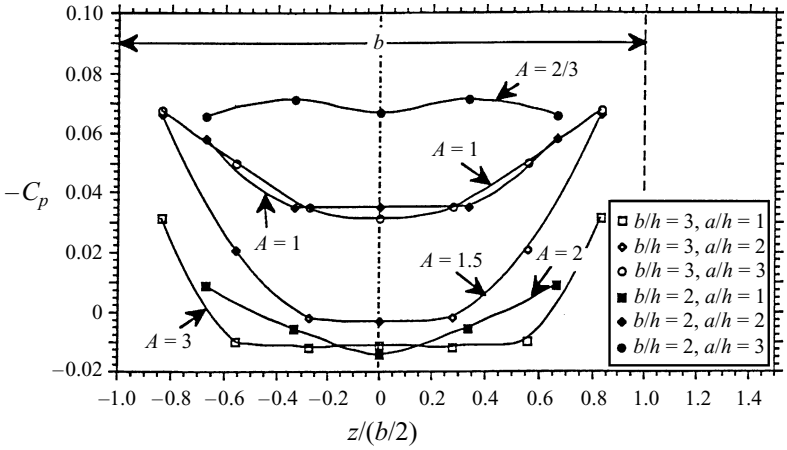

FIGURE 6. Spanwise pressure distribution on the top surface of the projection element for different aspect ratios

as a function of spanwise location. These results graphically demonstrate the influence of aspect ratio of castellations. The expansion fan emanating from the corner of the recess has a cone of influence across the top surface of the projection. The influence of the recess on the separating flow past the top surface of the projection is, therefore, increased as the aspect ratio becomes smaller. The results for $A = 2/3$ show that the pressure distribution just prior to separation has lower pressures with smaller gradients. This would suggest that the separating flow is influenced by both the adjacent recess regions.

The recompression shock behind the recess originates approximately two base heights downstream. This length is significant since it marks the position where further increases in castellation depth start having a reduced effect on the recess base pressure. Thus, for castellations of depth more than two base heights ($a/h > 2$), the recess flow upstream of the wake shock is isolated from the downstream influence so that the recess pressure is relatively independent of the castellation depth. The higher pressure in the recess downstream of the wake shock then provides an adverse pressure gradient to the flow separating from the projection tips.

Finally, base pressure measurements from the taps located off the spanwise axis (z)

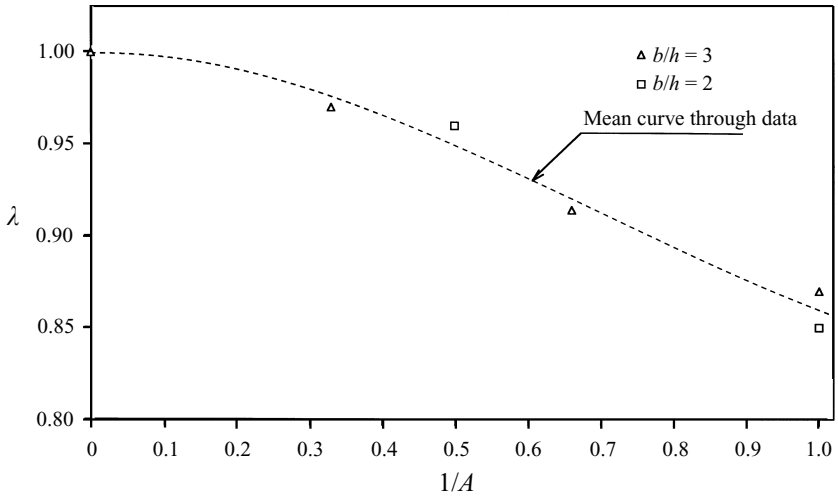

FIGURE 7. Relative base pressure coefficient as a function of aspect ratio.

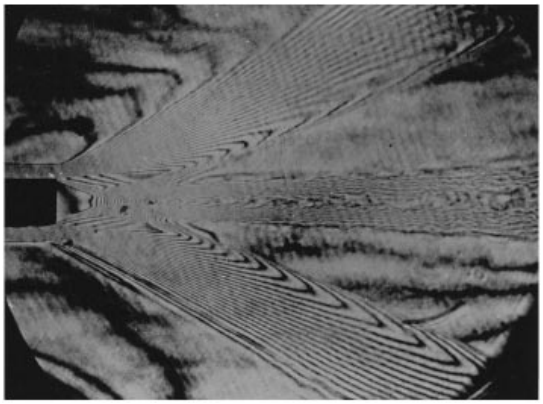

FIGURE 8. Finite fringe holographic interferogram of the flow behind a plain blunt trailing edge.

of the base, at 1 mm and 2 mm pitch, indicated that the transverse pressure gradient across the base thickness was negligible both in the case of the plain and the castellated base. This was also supported by Pitot pressure measurements 0.25 mm from the trailing edge.

3.2.2 *Influence of aspect ratio*

The measurements described above show that the base pressure recovery with a castellated base is a strong function of the aspect ratio of castellation elements. Figure 7 shows the relative base pressure coefficient λ plotted against the inverse of the aspect ratio A. λ is defined as the ratio of the mean base pressure coefficient of the castellated trailing edge to that of the plain blunt trailing edge, so that $(1-\lambda)$ gives a measure of the base pressure recovery.

We see that, in general, the pressure recovery improves as the aspect ratio becomes smaller and the trend of the data suggests that for maximum pressure recovery the aspect ratio would be of order unity. With the limited data that are available, nothing more definite can be said at present. We also see that as a measure of base pressure recovery, the castellation aspect ratio rather than the castellation width is a suitable parameter.

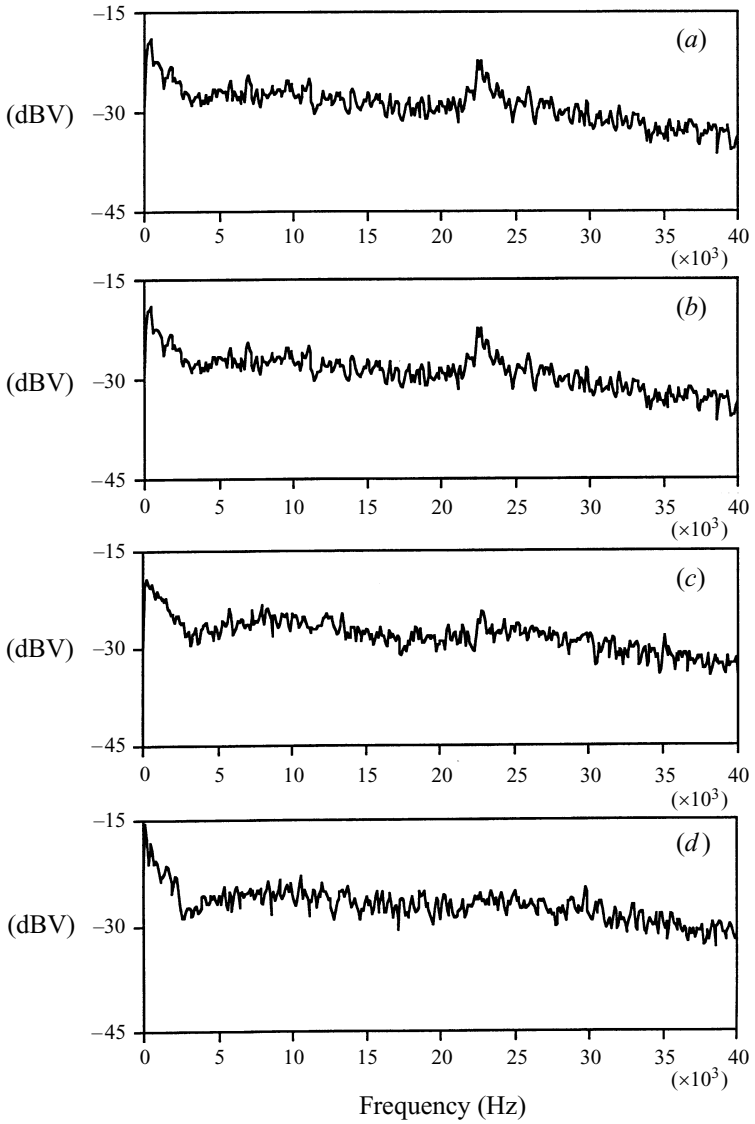

FIGURE 9. Frequency spectra of the flow behind a plain blunt trailing edge. (*a*) $Re = 25 \times 10^6$ m^{-1}, (*b*) 38×10^6, (*c*) 51×10^6, (*d*) 64×10^6.

That the optimum value of the aspect ratio is of the order unity is also supported by the results of Steen (1975). Steen did his experiments under similar flow conditions of Mach number and Reynolds number ($M_\infty = 2.0$ and $Re_L = 5 \times 10^6$) and varied the parameters a and b independently. He found that for maximum pressure recovery, $a/h \approx b/h \approx 2.4$. However, Steen states that while his results are qualitatively valid, large uncertainties in experimental data preclude any firm conclusions from being drawn. From the present experiments too it would seem that the optimum dimensions for the castellations are $2 \leqslant a/h \leqslant 3$ and $2 \leqslant b/h \leqslant 3$.

3.3. *Flow visualization studies*

Flow visualization studies were conducted with both the plain and the castellated blunt-trailing-edge aerofoils. These included schlieren photography, shadowgraphs

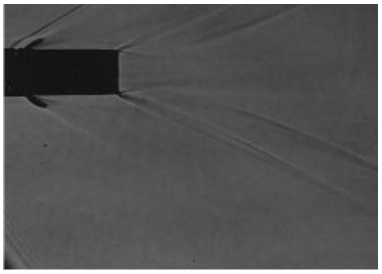

FIGURE 10. Shadowgraph of the flow behind a castellated trailing edge ($A = 1$).

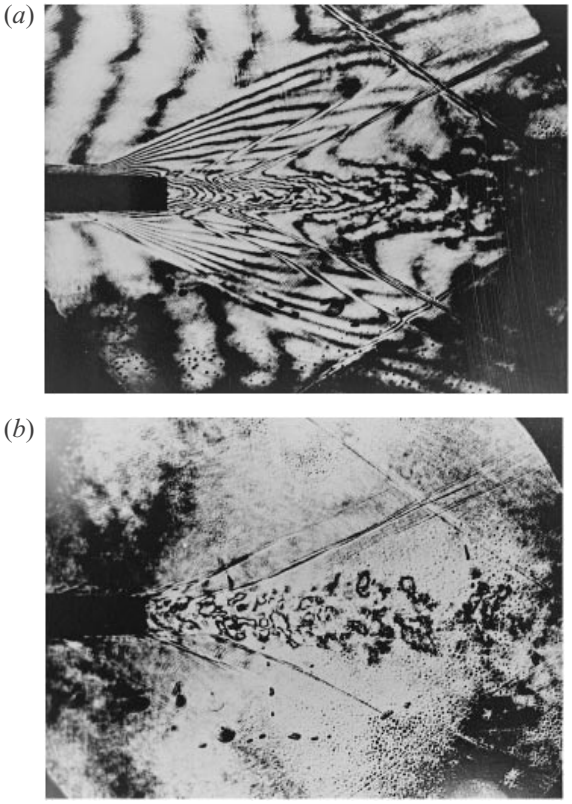

FIGURE 11. Holographic interferogram of the flow behind a castellated blunt trailing edge, $A = 1$: (*a*) infinite fringe; (*b*) differential.

and holographic interferometry, looking at the near-wake flow, both streamwise and spanwise. Some oil flow studies were also undertaken to examine the details of the flow on top of the projection boundary. The full details, describing the various optical set ups and data acquisition, are given in Magi (1990). In all the photographs discussed below, the flow is always from left to right.

3.3.1. *The plain blunt trailing edge*

As seen in figure 2, a weak lip shock emanates from the corner of the trailing edge into the expansion fan. The lip shock which is initially directed towards the wake axis starts to curve away from the wake axis just prior to the wake re-compression shock. The wake shock is located behind the re-circulation region approximately one to two

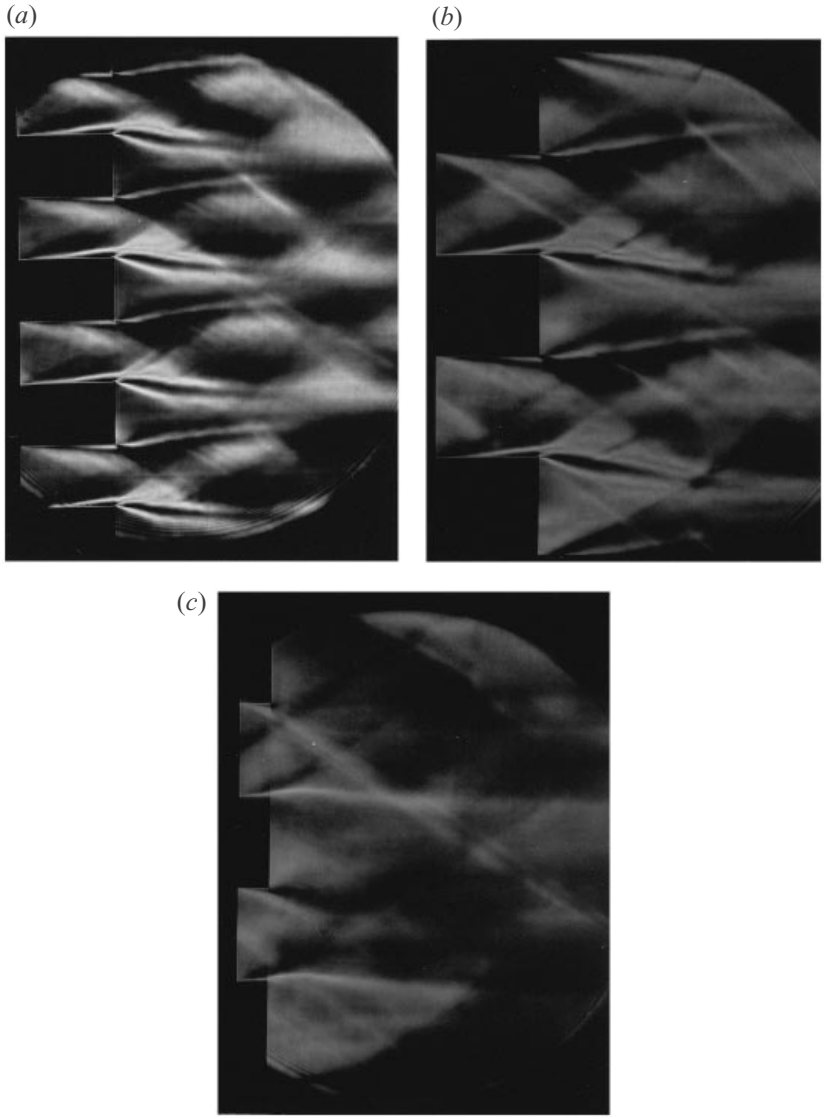

FIGURE 12. Schlieren photograph showing spanwise flow, sensitive to variation of density in the spanwise direction: (*a*) $A = 2/3$; (*b*) $A = 1$; (*c*) $A = 3$.

base heights downstream of the trailing edge and the wake shock emanates from the wake neck. If we assume that there is no pressure gradient across the free shear layer, we can get an estimate of the base pressure from the flow deflection. This yields a value of $C_{p_b} = -0.231$ which agrees well with both the pressure data and theoretical prediction.

Figure 8 shows a finite fringe holographic interferogram of the plain base flow. The interferogram shows that the lip shock terminates the expansion fan. The fringes change orientation from being radially aligned with the expansion corner to being aligned with the separated flow behind the base as we cross the lip shock. Since the fringes correspond to integrated optical density, we can clearly see the delineation of compressive and expansive regions that include the shear layer, the wake shock, the wake neck, and also the structure of the wake downstream.

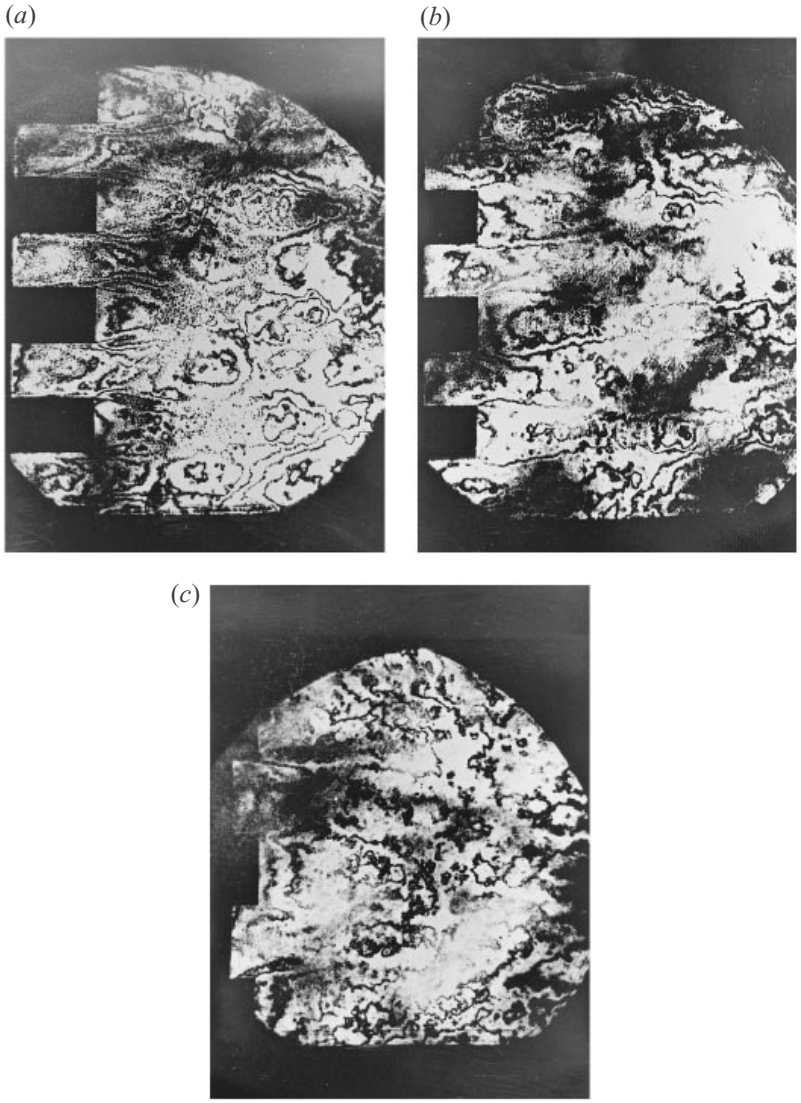

FIGURE 13. Infinite fringe holographic interferograms of spanwise flow.
(*a*) $A = 2/3$; (*b*) $A = 1$; (*c*) $A = 3$.

The wavy form of the fringe lines downstream of the neck indicates the presence of large-scale structures which are temporal and Reynolds number dependent. It is well known that periodic vortex shedding, while strong at subsonic and transonic speeds, is weak at high Mach numbers (Thomann 1959; Motallebi & Norbury 1981). It has been shown that the turbulent base flow at supersonic Mach numbers is stable and, in the wake downstream of the neck and the recompression shock, large-scale turbulent structures are found (Thomann 1959). This has also been effectively demonstrated by Althaus (1990) wherein the wake behind a smooth flat plate with a blunt trailing edge at a free-steam Mach number of 2.2 showed no distinct periodic vortex shedding but turbulent structures that were essentially random.

Frequency spectra obtained with a Kulite pressure probe placed at the edge of the wake and about 15 base heights downstream are shown in figure 9 for various

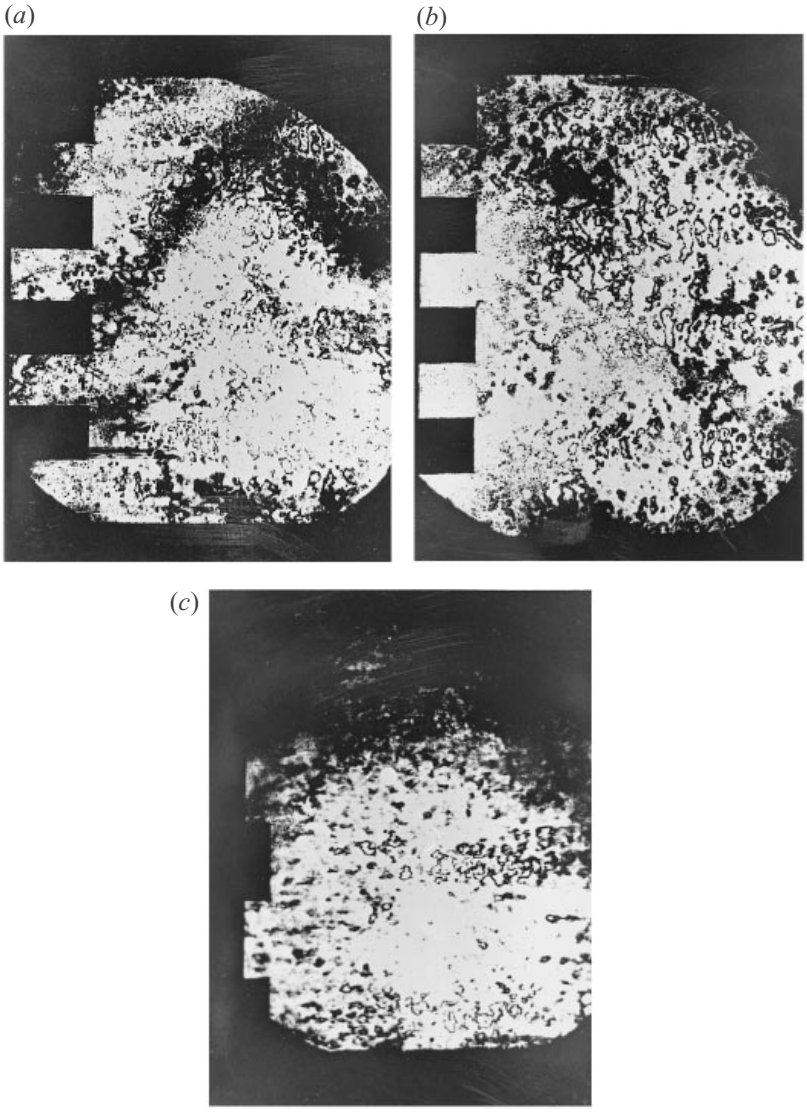

FIGURE 14. Differential holographic interferograms of spanwise flow.
(*a*) $A = 2/3$; (*b*) $A = 1$; (*c*) $A = 3$.

Reynolds numbers. Although a distinct frequency (≈ 22.6 kHz) can be picked up at the lower Reynolds numbers of 25×10^6 and 38×10^6 m^{-1}, it disappears at the higher Reynolds numbers. Considering that most of the experiments were done at unit Reynolds numbers between 60×10^6 and 70×10^6, no periodic shedding was evident. Motallebi & Norbury (1981) also found that at moderate supersonic Mach numbers ($M \approx 1.3$) the hot-wire signals showed periodicity of low amplitude and their schlieren photographs of the near wake of a blunt base show large-scale structures similar to the present ones.

3.3.2. *The castellated trailing edge*

Figure 10 shows a typical shadowgraph of the flow behind a castellated blunt trailing edge model. We notice that the wake neck is significantly thicker than that of the plain

blunt trailing edge and the wake shocks appear to form further away from the axis. The 'upstream' wake shock corresponds to that from behind the recess and the 'downstream' one corresponds to the one behind the projection. The origin of these is approximately two base heights behind their respective base.

The 'infinite' fringe and the 'differential' holographic interferogram of a castellated blunt trailing edge are shown in figures 11(*a*) and 11(*b*). Considering figure 11(*a*) first, we see again the orientation of the fringes changing behind the base after the expansion fan and the subsequent emergence of the wake recompression shock. We can also identify the diffused nature of the wake neck and the turbulent wake downstream. Figure 11(*b*), which is a differential holographic interferogram of the same flow, shows that the wake is characterized by well-defined oblique large-scale structures. Existence of these large-scale structures in supersonic turbulent wakes of blunt bodies, although has been noted before (Thomann, 1959), has not been identified and commented upon as such (Gai *et al.* 1997).

Now, looking at the spanwise flow, the schlieren photograph shown in figure 12(*a*), indicates a highly three-dimensional wake with strong gradients in the spanwise direction. Due to the discontinuous nature of the trailing edge, a spanwise pressure gradient is set up between the base region of the recess and the top surface of the projection. Some of the flow over the top of the projection is then entrained into the recess as a result of this pressure gradient. The separated flow in the recess is consequently recompressed and a weaker compression shock emanates from the neck region.

The base pressure on the projection is also characterized by a large spanwise gradient with lowest pressures at the edges. This gradient is a result of the mass entrained from the top surface of the projection into the recess as mentioned above. The wake shock behind the projection is formed further downstream than that behind the recess. A pressure mis-match, therefore, occurs between the outflow from the recess and the corner of the projection. The flow from the recess expands around the projection edge and the wake is characterized by a series of compression and expansion waves. It is seen that the flow pattern is similar to a series of under- and over-expanded jets. Also, the spanwise gradients seem to persist several base heights downstream. Figures 12(*b*) and 12(*c*) show similar features but with different aspect ratio castellations. It is clear from comparison of photographs 12(*a*), 12(*b*), and 12(*c*), that spanwise gradients become stronger with decrease in aspect ratio.

Figure 13 shows some examples of infinite fringe holographic interferograms of the spanwise flow. Firstly, they show unsteady vortex-ring-like structures behind the projections which seem to become more organized with the decrease in castellation aspect ratio. Secondly, as the castellation aspect ratio decreases, the interaction between these structures increases, generating stronger gradients.

The differential interferograms, shown in figure 14, illustrate the unsteady structures seen here as fringe loops consistent with vortex structures. They appear elongated suggesting spanwise stretching.

Oil flow visualization studies confirmed the existence of a spanwise gradient. Figure 15 shows a typical oil flow pattern on a projection element. The oil tracks clearly show that a spanwise gradient exists and that the fluid is drawn from the top of the projection into the recess. The fluid thus entrained is approximately bounded by the leading characteristic of the expansion fan emanating from the corner of the recess trailing edge and the recess/projection boundary. The influence of the recess appears to extend approximately the order of a boundary layer thickness (2 mm) across the projection span inboard of the leading characteristic.

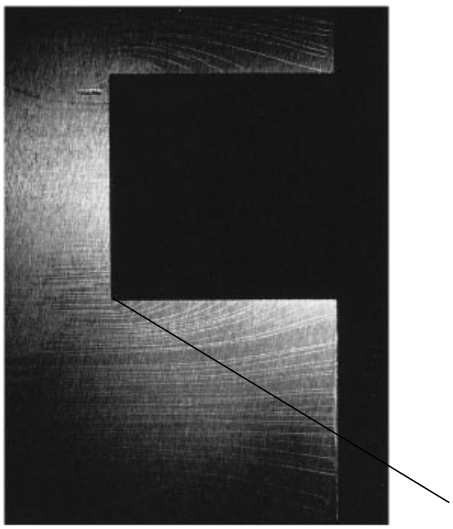

FIGURE 15. Oil flow pattern on a projection element ($A = 1$).

3.4. *Laser transit velocimetry (LTV) results*

The combination of high-velocity, highly turbulent, three-dimensional flows with difficult access such as are encountered behind castellated blunt-trailing-edge aerofoils makes acquisition of quantitative point measurements in the near wake especially difficult. A non-intrusive optical diagnostic such as the laser doppler anemometer (LDV) is the tool often used to obtain such quantitative data. However, the more recently developed laser transit velocimetry (LTV), which measures the time of flight of suspended seed particles between two narrowly focused laser beams (hence sometimes referred to as laser two-focus velocimetry) offers advantages in high-speed flows particularly if limited optical access restricts operation to backscatter mode and where measurements are made close to solid surfaces. The transit time of a convected seed particle between the two focii of the LTV is large compared to the transit time between the virtual interference fringes of an LDV. Hence, for a system with finite temporal resolution, higher velocities can be measured with the LTV. Secondly, the optical configuration of the LTV permits sharper focusing of beams at the measuring point resulting in increased intensity of scattered light and improved spatial resolution. These advantages render LTV more attractive in situations where problems of high speeds, limited access, and proximity to solid surfaces, are all encountered.

The LTV has been used in the past as a diagnostic tool to measure velocities and turbulence intensities in high transonic flows. Its use here at supersonic speeds and under three-dimensional flow situations is somewhat new. The results must therefore be viewed with caution and they are presented here only to complement pressure and flow visualization data.

The LTV system used was a Polytec system with a 2.5 W argon-ion laser and a signal processor. The beam diameter at the focal plane was 10 μm and the beam separation was 225 μm. No artificial seeding was needed as the system was sensitive enough to detect particles of size as small as 0.1 μm (Schodl 1980).

The theory of operation of the LTV system has been described elsewhere (Prytz 1989). Figures 16(*a*) and 16(*b*) show the optical head and the arrangement of focal volumes with their orientation. Briefly, the light scattered by particles passing through the two focii is sensed by two photomultipliers, one for each focus. The signal from

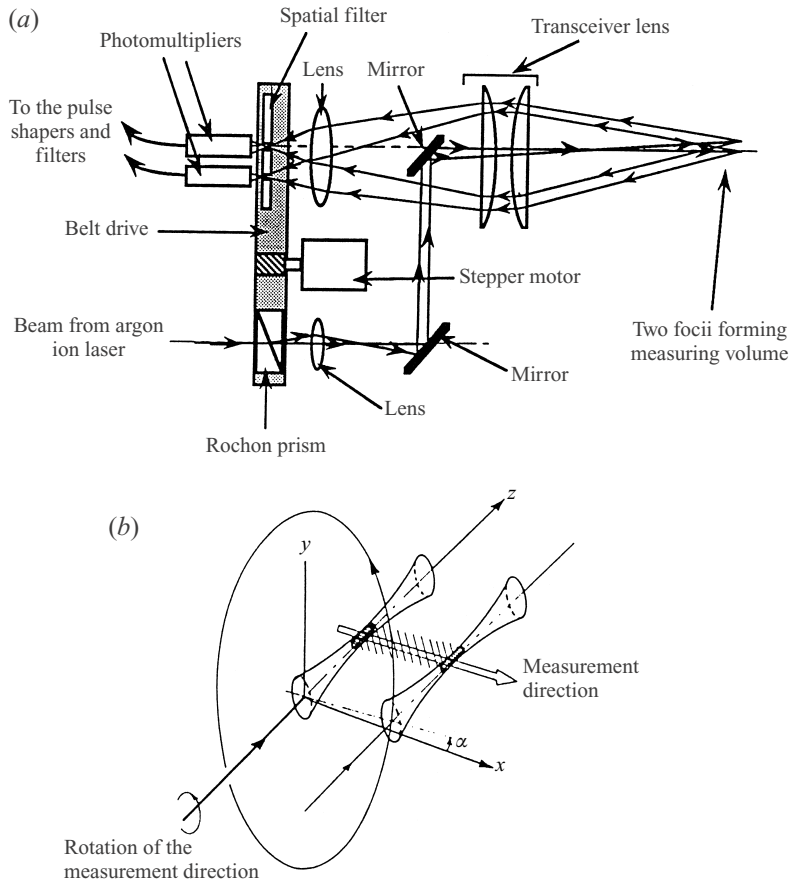

FIGURE 16. Laser transit velocimeter: (*a*) optical head; (*b*) focal volumes and measurement direction.

each focus is amplified and the time of flight of a particle is then measured by a time-to-pulse height converter (TPHC) which generated an output pulse proportional to the time interval between a start and stop pulse. The output of the TPHC is then digitized by a multi-channel analyser which produces a histogram of times of flight, from which the velocity distribution is derived. The details of extracting turbulence data from stochastic analysis of basic measurements are described by Prytz (1989). The accuracy of velocity and turbulence measurements is estimated to be $\pm 4\%$ and $\pm 12\%$ respectively. In the present set up, the beam was traversed across the wake by placing the laser system on a milling machine platform and traverses were possible in all the three coordinate directions.

Velocity and turbulence measurements in the boundary layer and wakes behind a plain blunt and a castellated base were made at selected locations (see figure 17). The wake measurements were made along the centrelines of the projection and recess for the castellated model and along the centreline of the plain base model. Measurements were also made at different spanwise (z) locations. Boundary layer traverses were made at the separation edge for both trailing edges as shown in figure 17.

Figure 18(*a*) shows the measured boundary layer profiles. The profiles approximate the 1/7th power law profile and the boundary layer thickness is in agreement with the Pitot traverse data. Figure 18(*b*) shows the longitudinal turbulence intensity profiles

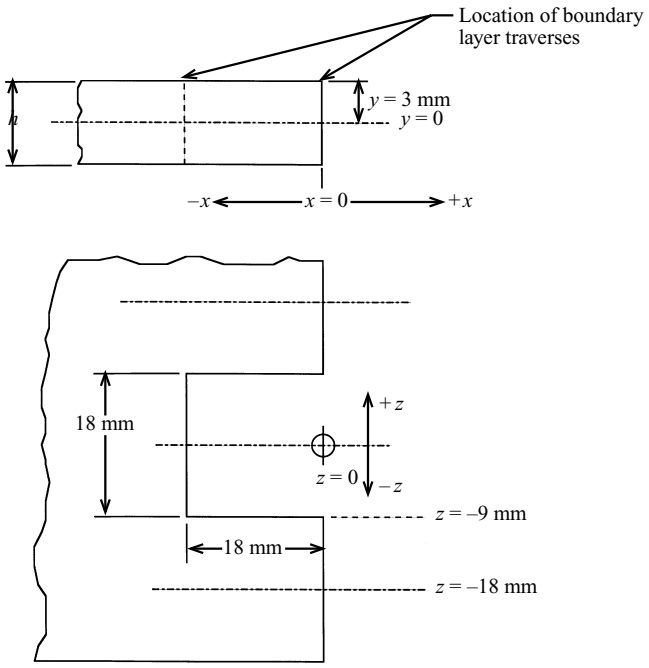

FIGURE 17. Schematic showing locations of boundary layer and wake traverses.

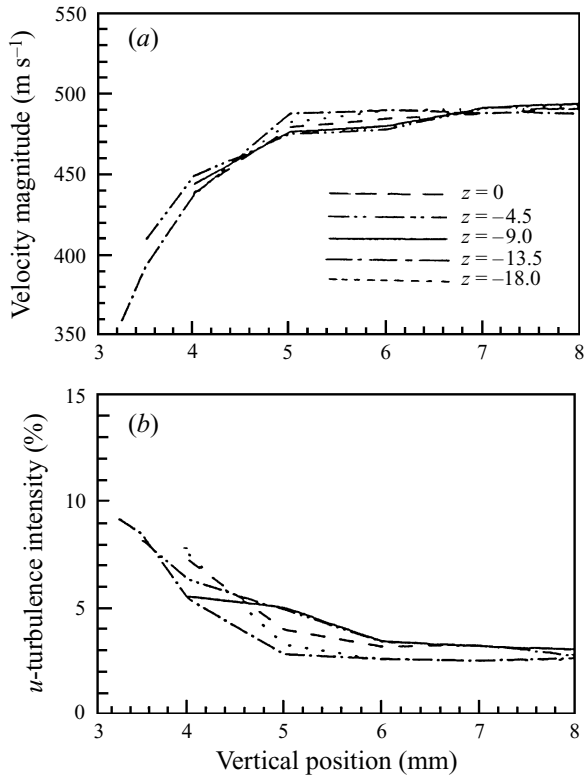

FIGURE 18. Boundary layer measurements: (*a*) mean velocity; (*b*) longitudinal turbulence intensity.

and we note that the turbulence intensity close to the surface is high, decreasing rapidly away from the surface (see Young 1989). It should be noted that the vertical position of 3 mm in figure 18 corresponds to the surface of the model (see figure 17).

Figure 19(*a–c*) shows the mean velocity contour map behind the plain blunt trailing edge and behind the projection and recess of a castellated trailing edge. Considering the plain base and the projection of a castellated trailing edge, we note the boundary layer, the expansion fan, the lip shock and a clearly defined wake neck. The neck is broader behind the projection of the castellated trailing edge, consistent with the results of flow visualization data. The results for the recess show the boundary layer at the separation edge, and the expansion fan thereof, quite clearly. The neck details behind the recess are obscured by the projection and could not be measured.

Figure 20(*a–c*) shows the longitudinal turbulence intensity behind the plain and the castellated blunt trailing edges. Considering the plain blunt trailing edge first, figure 20(*a*), we note relatively high turbulence intensities in the boundary layer near the surface which further increase in the separated region behind the base with a well-defined neck about a base height downstream. The presence of the expansion fan, with the turbulence intensity decreasing away from the corner may be noted. The increase in turbulence intensity level due to the lip shock is also evident. It is seen that in the boundary layer near the surface the turbulence intensity is about 8 %, while in the free stream it is reduced to about half this value. In the separated region it is consistently high to about 8 %. These trends are similar to those measured in other supersonic separated flows using laser velocimetry (Modarress & Johnson 1979; Baroth & Holt 1983). The lateral turbulence intensity measurements $\langle v' \rangle$, shown in figure 21(*a*), are similar; however, the magnitudes of lateral turbulence intensities are somewhat higher. Similar results, wherein the lateral turbulence intensities $\langle v' \rangle$ were higher than the longitudinal turbulence intensities $\langle u' \rangle$, in LTV measurements of moderate turbulence intensity flows, have been noted before (Lai & He 1989). Lai & He (1989) attribute this to the fact that the measurement direction determined by the two focal points may not truly represent the actual ensemble-average velocity of the particles recorded at a particular angular position and that at angular positions far away from the local mean flow direction, the time-of-flight histograms may contain higher statistical noise than those obtained at angular positions closer to the mean flow direction.

The longitudinal turbulence intensities behind the projection and the recess are shown in figure 20(*b*, *c*). It is interesting to note that while the magnitudes are similar to that of the plain blunt trailing edge, the gradients are smaller with a wider wake, consistent with the flow visualization evidence. The lateral turbulence intensity measurements $\langle v' \rangle$, shown in figure 21(*b*, *c*), are once again similar but with magnitudes slightly higher.

Looking at the turbulence intensities along the spanwise direction, shown in figure 22, on the centreline of the recess ($z = 0$), there is a larger gradient where there are pockets of low turbulence in the outer shear layer and high turbulence in the separated region behind the trailing edge of the recess. This is the result of expansion and the entrainment of the fluid from the top of the projection into the recess as described earlier. In contrast, the turbulence intensities along the centreline of the projection ($z = 18$) are more uniformly distributed showing clearly the effect of expansion in the outer flow and high values within the boundary layer. The turbulence intensities at the recess/projection edge ($z = -9$) show, again, large gradients indicating strong expansion in the outer flow with pockets of high turbulence. We also notice the influence of the recess flow extending on to the top of the projection consistent with the oil flow and pressure data.

Again, the results of $\langle v' \rangle$ fluctuations showed similar trends but their magnitudes were slightly higher because, as pointed out above, the signal to statistical noise ratio is reduced with both increasing turbulence intensity and sampling rate.

It is also worth noting that the levels of turbulence intensities are considerably less than those measured in the wakes of both plain and castellated blunt-trailing-edge aerofoils in subsonic flows. In a parallel investigation of flow behind castellated blunt-trailing-edge aerofoils at subsonic speeds, Petrusma (1990) found streamwise and lateral turbulence intensity levels, $\langle u' \rangle$ and $\langle v' \rangle$ respectively, to be of the order of 20%. This is consistent with the well-known fact that a decrease in turbulence levels occurs with increase in Mach number (Smits & Dussauge 1996).

4. A simple model to predict the mean base pressure coefficient on a castellated blunt trailing edge

This model predicts the mean base pressure for both the recess and projection elements of a castellated blunt base. It is based on the premise that the base pressure recovery of a castellated blunt trailing edge is primarily due to the segmentation of the flow and the 'bleed effect' of the flow into the recess region from the sides of the projection (Magi 1990). The model incorporates several elements of Tanner's (1973, 1984) subsonic and supersonic steady base pressure theories pertaining to both two-dimensional and axisymmetric flows. Considering the complicated and the quasi-steady nature of the flow behind a castellated blunt trailing edge, the model involves numerous assumptions and simplifications and as such can only be considered as approximate.

4.1. *Base pressure in the recess region*

For the recess, it is assumed that the flow can be modelled as a two-dimensional flow with 'base bleed'. The bleed effect is obtained by the entrainment of fluid from the projection surface (see figures 15 and 23). The base pressure coefficient is then obtained by applying Tanner's (1973) second outflow function to the wake. This function satisfies the mixing requirements in the free shear layer through the continuity and momentum equations for the recirculation and free shear layer regions.

Tanner (1973, 1984) proposed that there is a connection between the mass outflow from the re-circulation region and the base pressure. Referring to figure 24, the mass flux through the boundary AC is given by

$$m_a = \int_0^{da} \rho U \, \mathrm{d}y'. \tag{1}$$

In dimensionless form, it is

$$C_{qa} = \frac{m_a}{\rho_\infty U_\infty h} = \frac{\rho_2 U_2 \, ds}{\rho_\infty U_\infty h} \int_0^{ds/da} \frac{\rho U}{\rho_2 U_2} \mathrm{d}\zeta, \tag{2}$$

where $\zeta = y'/ds$ and ds is the free shear layer thickness measured in the y' direction.

The momentum equation can be shown to satisfy the relation

$$\int_0^{ds} \rho U^2 \, \mathrm{d}y' - U_2 \int_{da}^{ds} \rho U \, \mathrm{d}y' = 0, \tag{3}$$

which in dimensionless form is

$$\int_0^1 \frac{\rho U^2}{\rho_2 U_2^2} \mathrm{d}\zeta - \int_{da/ds}^1 \frac{\rho U}{\rho_2 U_2} \mathrm{d}\zeta = 0. \tag{4}$$

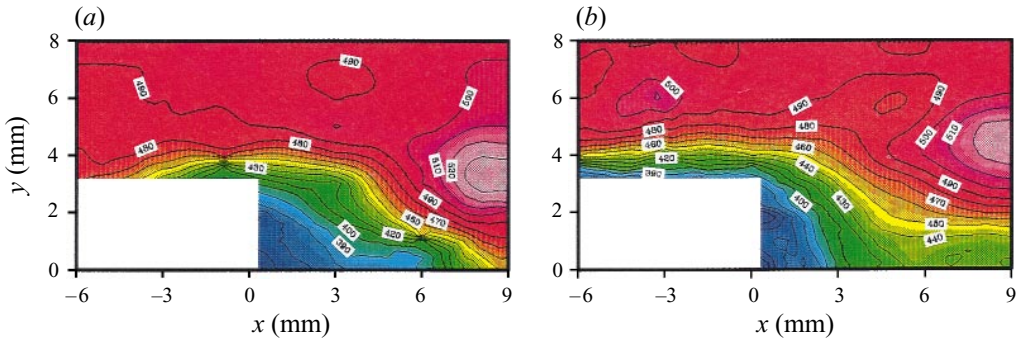

FIGURE 19 (*a*, *b*). For caption see facing page.

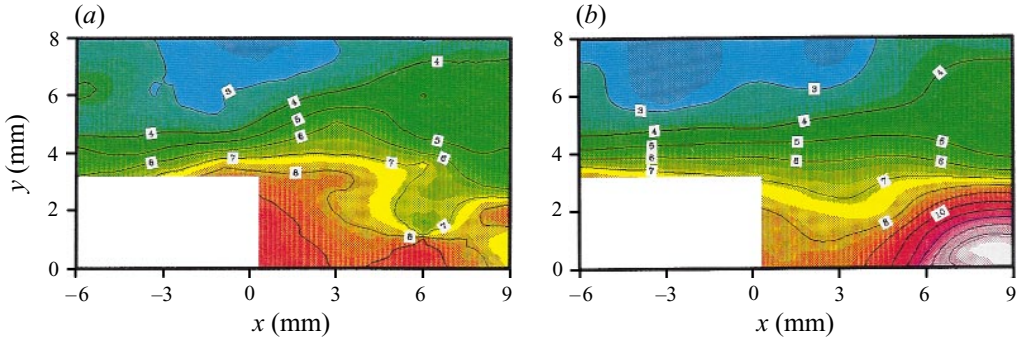

FIGURE 20 (*a*, *b*). For caption see facing page.

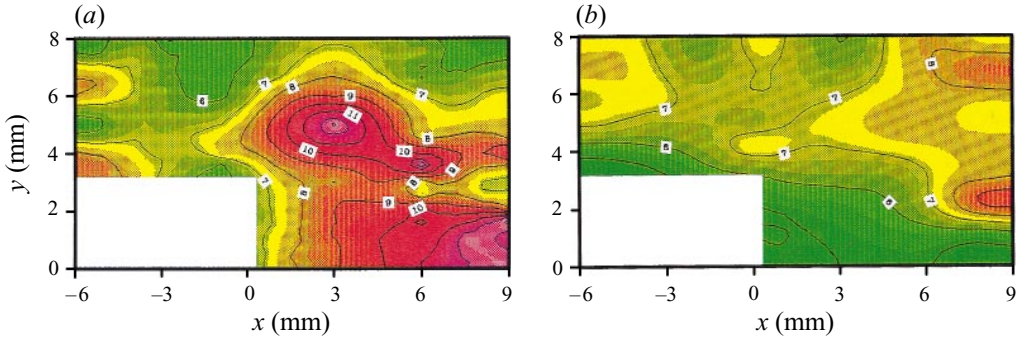

FIGURE 21 (*a*, *b*). For caption see facing page.

For a given free-stream Mach number and base pressure, (4) gives a unique value for da/ds and hence (2) can be solved.

We assume that the bleed mass flow can be described in terms of the ratio b'/b and, to a first approximation, it is given by (see Magi 1990)

$$\left(\frac{C'_{qa}}{C_{qa}}\right) \approx \left(\frac{b+2b'}{b}\right), \tag{5}$$

where C'_{qa} is the dimensionless mass outflow for an equivalent two-dimensional flow with base bleed, C_{qa} is the dimensionless mass outflow from a plain base and b' is the limiting value of b^* (figure 25), such that

$$b' = \lim_{a' \to a} (b^*).$$

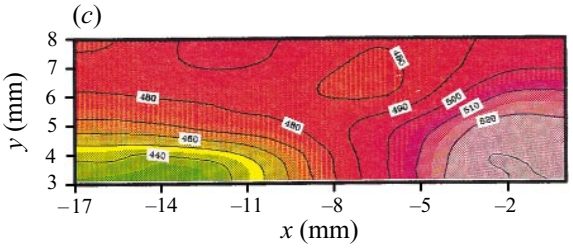

FIGURE 19. Mean velocity contours (m s^{-1}): (*a*) plain blunt trailing edge; (*b*) centreline of projection of castellated trailing edge; (*c*) centreline of recess of castellated trailing edge.

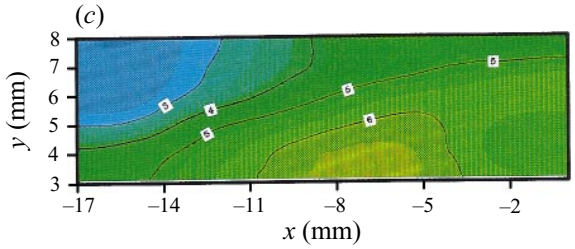

FIGURE 20. Longitudinal turbulent intensity distribution (%): (*a*) plain blunt trailing edge; (*b*) centreline of projection of castellated trailing edge; (*c*) centreline of recess of castellated trailing edge.

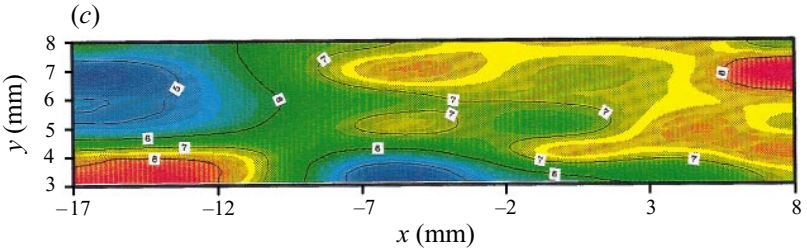

FIGURE 21. Lateral turbulent intensity distribution (%): (*a*) plain blunt trailing edge; (*b*) centreline of projection of castellated trailing edge; (*c*) centreline of recess of castellated trailing edge.

It is further assumed that the entrained flow from the projection surface has only a small effect on the growth of the free shear layer, so that

$$\left(\frac{C'_{qa}\,ds/h}{C_{qa}\,ds/h}\right) \approx \left(\frac{C'_{qa}}{C_{qa}}\right). \tag{6}$$

The flow on the surface of the projection may be approximately considered to be locally two-dimensional and the ratio b'/b is estimated using inviscid flow theory, giving

$$\frac{b'}{b} = \frac{1}{AM_\infty}\left(\frac{1+\frac{1}{2}(\gamma-1)\,M_\infty^2}{1+\frac{1}{2}(\gamma-1)\,M_{2'}^2}\right)^{\frac{\gamma+1}{2(\gamma-1)}}\left(\frac{1}{\cos\phi\,(1+\tan\phi/\tan\theta)}\right) \tag{7}$$

or

$$\frac{b+2b'}{b} = 1+\frac{2}{AM_\infty}\left(\frac{1+\frac{1}{2}(\gamma-1)\,M_\infty^2}{1+\frac{1}{2}(\gamma-1)\,M_{2'}^2}\right)^{\frac{\gamma+1}{2(\gamma-1)}}\left(\frac{1}{\cos\phi\,(1+\tan\phi/\tan\theta)}\right), \tag{8}$$

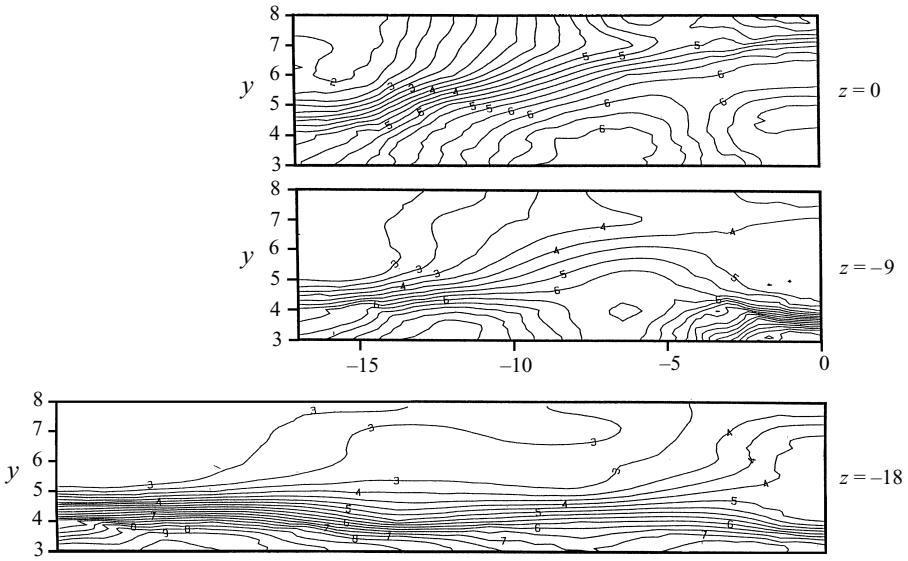

FIGURE 22. Spanwise longitudinal turbulent intensity distribution behind a castellated trailing edge: (*a*) along the centreline of recess; (*b*) at recess/projection boundary; (*c*) along the centreline of projection.

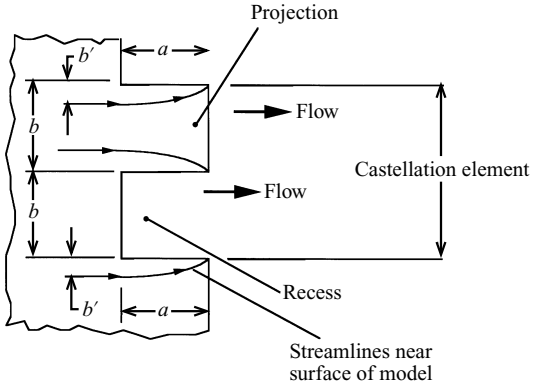

FIGURE 23. Sketch of streamlines in the vicinity of a castellation element.

where $A = b/a$ is the aspect ratio of the castellation; ϕ and θ are as defined in figure 25. $M_{2'}$ is the separation Mach number from the recess/projection edge downstream of the expansion fan (figure 25).

Equation (7) shows that as $A \to \infty$, the ratio b'/b tends to zero, that is, the flow becomes two-dimensional. However, as $A \to 0$, the equation becomes indeterminate. To take account of this, we modify equation (8) by writing

$$\frac{b+2b'}{b} = 1 + f_1 G_1, \tag{9}$$

where

$$f_1 = \frac{2}{AM_\infty}\left(\frac{1+\frac{1}{2}(\gamma-1)M_\infty^2}{1+\frac{1}{2}(\gamma-1)M_{2'}^2}\right)^{\frac{\gamma+1}{2(\gamma-1)}}\left(\frac{1}{\cos\phi\,(1+\tan\phi/\tan\theta)}\right)$$

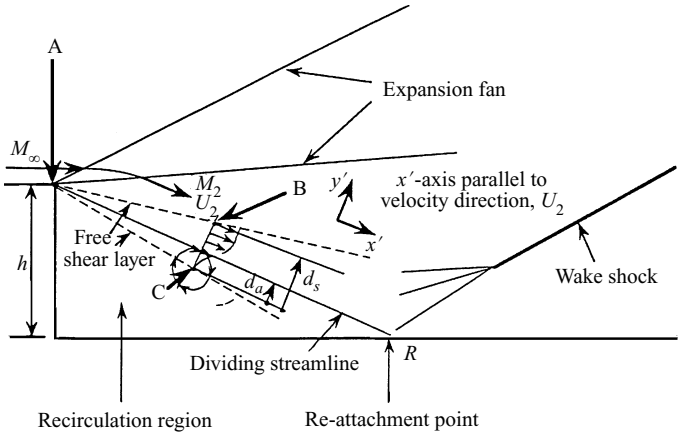

FIGURE 24. Schematic of a steady supersonic base flow (after Tanner 1984).

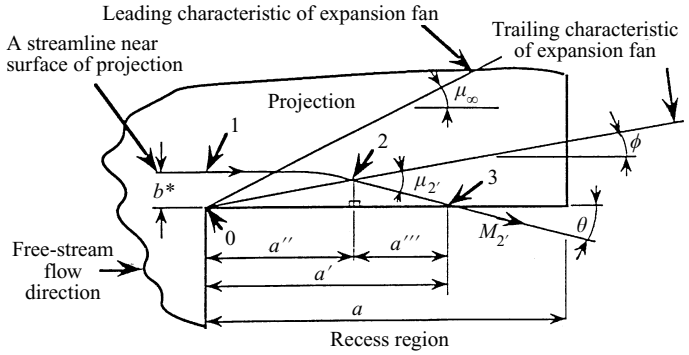

FIGURE 25. Schematic of flow near projection/recess boundary.

and

$$G_1 = \frac{2}{\pi}\tan^{-1}\left(\frac{3\pi}{4}A\right)$$

which satisfies the boundary conditions $A = \infty$ and $A \quad 1$. Then

$$\frac{b'}{b} = \frac{2\tan^{-1}(\frac{3}{4}\pi A)}{\pi A M_\infty}\left(\frac{1+\frac{1}{2}(\gamma-1)M_\infty^2}{1+\frac{1}{2}(\gamma-1)M_{2'}^2}\right)^{\frac{\gamma+1}{2(\gamma-1)}}\left(\frac{1}{\cos\phi\,(1+\tan\phi/\tan\theta)}\right). \tag{10}$$

The full details are given in Magi (1990).

Using Tanner's (1984) approach, a unique relationship exists between the dimensionless mass outflow function $C_{qa}/(ds/h)$ and the base pressure coefficient. Thus, from equation (10), the dimensionless mass outflow function for an equivalent two-dimensional base flow with base bleed can be calculated using equations (5) and (6). Then finally, the base pressure coefficient is determined from

$$C_{pb} = \frac{2}{\gamma M_\infty^2}\left(\left(\frac{1+\frac{1}{2}(\gamma-1)M_\infty^2}{1+\frac{1}{2}(\gamma-1)M_{2e}^2}\right)^{\frac{\gamma}{\gamma-1}} - 1\right), \tag{11}$$

where M_{2e} is the separation Mach number of the equivalent two-dimensional base flow. It should be noted that the separation Mach number M_2, at the recess/projection boundary is, in general, not quite equal to M_{2e} but is close.

For the fluid to be entrained from the top of the projection and into the recess, a spanwise pressure gradient must exist between the recess region and the projection. If the expansion fan from the recess lies along the recess/projection edge (i.e. $\phi = 0°$), then at $M_\infty = 2.0$, the corresponding flow deflection θ will be 20.5° as against the two-dimensional flow deflection of 16.4°, giving a base pressure coefficient of -0.23. This would indicate that the pressure at the recess/projection edge is lower than the recess pressure which is consistent with the measurements.

4.2. *Modelling of the mean base pressure on the projection*

In what follows the mean base pressure is modelled as a combination of two-dimensional and axi-symmetric flow to take account of the effects of three-dimensional nature of the base flow over the projection. The mean base pressure coefficient on the projection, $(C_{p_b})_p$, is assumed to be of the form

$$(C_{p_b})_p = S_t C_t + S_x C_x, \tag{12}$$

where subscripts t and x refer to two-dimensional and axi-symmetric components respectively. S is a scaling function and C is a function containing the components of base pressure coefficients.

The separation Mach numbers in the present context differ from the free-stream Mach number due to the expansion fan from the corner of the recess/projection boundary. The separation Mach numbers used for the calculations here are obtained by integrating across the trailing edge of the projection element:

$$\langle M \rangle = \int M z \, \mathrm{d}z \Big/ \int z \, \mathrm{d}z, \tag{13}$$

where the z-axis is in the spanwise direction. The integration limits for $\langle M_t \rangle$ and $\langle M_x \rangle$ are determined by the scaling functions S_t and S_x. For large aspect ratios this is relatively easy. The Mach number at the trailing edge is determined from the position of the expansion fan. For low-aspect-ratio projections, the separating flow is non-simple. It is influenced by the expansion fan from the adjacent recess regions (see discussion in §3.2.1). The Mach number can, of course, be obtained by constructing a characteristic mesh on the top surface of the projection. However, an alternative approach was used here and is described below.

From the recess calculations, discussed above, we obtain values for $(b+2b')/b$. Since the recess and the projection have the same width, we know the value of the parameter $(b-2b')/b$ (figure 23). The flow is assumed to be locally two-dimensional, and the average Mach number M_{II} at separation is obtained, using the approximate expression

$$M_{II} = S_t \langle M_t \rangle + S_x \langle M_x \rangle. \tag{15}$$

As the aspect ratio $A \to 0$, $\langle M_t \rangle$ and $\langle M_x \rangle \to M_{II}$.

The scaling functions are assumed to be of the following form (Magi 1990):

$$S_t = \left(1 - \frac{h}{b} \sin^2\left(\frac{\pi a}{4h}\right)\right), \quad \text{where } 0 \leqslant a/h \leqslant 2,$$

$$S_t = \left(1 - \frac{h}{b}\right), \qquad \text{where } a/h \geqslant 2,$$

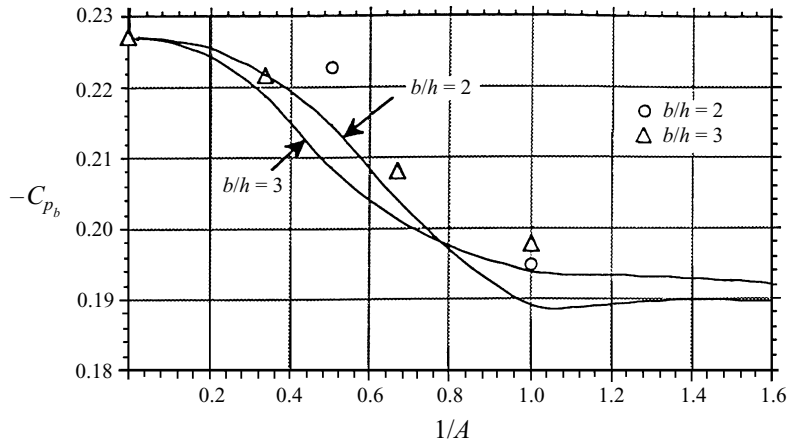

FIGURE 26. Mean base pressure coefficient as a function of aspect ratio: comparison between theory and experiment.

and

$$S_x = \frac{h}{b}\sin^2\left(\frac{\pi a}{4h}\right), \qquad \text{where } 0 \leqslant a/h \leqslant 2$$

$$S_x = \frac{h}{b}, \qquad \text{where } a/h \geqslant 2.$$

The functions C_t and C_x are in terms of base pressure coefficients and are given by

$$C_t(M_\infty) = \frac{2}{\gamma M_\infty^2}\left(\left(\frac{1+\frac{1}{2}(\gamma-1)\,M_\infty^2}{1+\frac{1}{2}(\gamma-1)\,M_{II}^2}\right)^{\frac{\gamma}{\gamma-1}}(1+\tfrac{1}{2}\gamma M_{II}^2\,C_{pb}(\langle M_t\rangle))-1\right),$$

$$C_x(M_\infty) = \frac{2}{\gamma M_\infty^2}\left(\left(\frac{1+\frac{1}{2}(\gamma-1)\,M_\infty^2}{1+\frac{1}{2}(\gamma-1)\,M_{II}^2}\right)^{\frac{\gamma}{\gamma-1}}(1+\tfrac{1}{2}\gamma M_{II}^2\,C_{pb}(\langle M_x\rangle))-1\right).$$

$C_{p_b}(\langle M_t\rangle)$ and $C_{p_b}(\langle M_x\rangle)$ are base pressure coefficients calculated using Tanner's (1984) supersonic base pressure theory.

4.3. *Comparison with experimental data*

Calculations, based on these models of the flow in the recess and the projection, were made for the mean base pressure coefficient as a function of aspect ratio at a free-stream Mach number of 2 and then compared with experimental data obtained for projection and recess widths of $b/h = 3$ and 2. The results are shown in figure 26. It is seen that the theory predicts qualitative features of the flow reasonably well, although it generally overestimates the pressure recovery obtainable with a castellated trailing edge. This is thought to be mainly due to the deficiencies in modelling. The theory also predicts that the base pressure coefficient asymptotes as the aspect ratio becomes small, indicating that, for maximum pressure recovery, the aspect ratio is around unity. This is consistent with the experimental findings shown in figure 7.

5. Conclusions

Drawing upon pressure, flow visualization, velocity and turbulence data, the nature of the flow behind plain and castellated blunt-trailing-edge aerofoils in supersonic flow has been investigated.

The results show that castellated trailing edges do yield pressure recovery over the plain base. This, together with the fact that castellated trailing-edge aerofoils have significant advantages in subsonic and transonic flows, means that they should be given serious consideration in the design of supersonic and transonic wings and control surfaces as well as turbine blades.

The drag reduction seems primarily due to the segmentation of the flow and the resulting spanwise gradients that are set up. In particular, there is an entrainment of the fluid from the top of the projection into the recess. This acts to increase the mean pressure in the recess. This pressure increase in the recess more than offsets the low-pressure region created at the recess/projection boundaries. Further, due to the segmentation of the base, the flow contains a series of weak shocks recompressing the flow back to the free-stream pressure instead of a single strong recompression shock, thus causing a smaller entropy increase and hence less drag. The wake shock also appears to form further away from the axis.

It has also been shown that the base pressure recovery is a strong function of the aspect ratio of the castellations. From the limited data of the present experiments, it appears that the optimum value of the aspect ratio of castellations for maximum pressure recovery at supersonic speeds is of the order of unity.

A flow model has been proposed to predict the mean base pressures on the projection and recess elements of a castellated trailing edge and the theory shows reasonable agreement with experimental data.

We thank Mr A. Tarnopolsky for providing us with the frequency spectra data shown in figure 9. We are grateful to the referees for their constructive criticism and helpful suggestions to improve the paper. Grateful acknowledgements are also due to the Australian Research Council who supported part of this work.

REFERENCES

Althaus, W. 1990 *Exps. Fluids* **9**, 267–272.

Baroth, E. C. & Holt, M. 1983 *Exps. Fluids* **1**, 195–203.

Bearman, P. W. 1965 *Aero. Q.* **18**, 207–224.

Bearman, P. W. *J. Fluid Mech.* **21**, 241–255.

Briedenthal, R. 1980 *Phys. Fluids* **23**, 1929–1934.

Chapman, D. R. 1951 *NACA Rep.* 1051.

Gai, S. L. & Sharma, S. D. 1981 *Aeronaut J.* **85**, 206–210.

Gai, S. L., Tarnopolsky, A., O'Byrne, S., Houwing, A. F. & Mudford, N. R. 1997 *Proc. 21st ISSW, July 21–25, Great Keppel, Australia,*

Hama, F. R. 1968 *AIAA J.* **6**, 212–219.

Holder, D. W. 1964 *J. R. Aero. Soc.* **68**, 501–516.

Hosking, P. R. & Self, D. Q. 1974 *Rep. 175.* Aero Engng Dept., University of Bristol.

Korst, H. H. 1956 *J. Appl. Mech.* **23**, 593–600.

Lai, J. C. S. & He, Y. 1989 *J. Phys.* E **22**, 225–231.

Magi, E. C. 1990 Investigations into the flow behind castellated blunt trailing edge aerofoils at supersonic speed. PhD. thesis, University College, Univ. of New South Wales, Australia.

Modarress, D. & Johnson, D. A. 1979 *AIAA J.* **17**, 747–752.

Motallebi, F. & Norbury, J. F. 1981 *J. Fluid Mech.* **110**, 273–292.

Petrusma, M. S. 1990 A near wake study of segmented blunt trailing edge aerofoils in subsonic flow. PhD thesis, University College, Univ. of New South Wales, Australia.

Petrusma, M. S. & Gai, S. L. 1994 *Aeronaut. J.* **98**, 267–278.

Pierrehumbert, R. T. & Widnall, S. E. 1982 *J. Fluid Mech.* **114**, 59–82.

POLLOCK, N. 1972 *ARL* (*Australia*) *Rep*. 137.

PRYTZ, A. 1989 '*A2F*' *Polytec L2F Hardware Program Rept*. Mech. Engng Dept., University College, UNSW, ADFA.

ROSHKO, A. 1993 *J. Wind Engng Ind. Aero*. **49**, 79–100.

SCHODL, R. 1980 *Trans. ASME: J. Fluids Engng* **102**, 412–419.

SMITS, A. J. & DUSSAUGE, J. P. 1996 *Turbulent Shear Layers in Supersonic Flow*. AIP Press.

STEEN, P. H. 1975 *Rep*. 183. Aero Engng Dept., Univ. of Bristol.

TANNER, M. 1972 *Aero. Q*. **23**, 15–23.

TANNER, M. 1973 *Prog. Aero. Sci.* **14**, 177–225.

TANNER, M. 1984 *Prog. Aero. Sci.* **21**, 81–157.

THOMANN, H. 1959 *Rep*. 84. *FFA*, *Sweden*.

YOUNG, A. D. 1989 *Boundary Layers*, p. 140. BSP Professional Books.